PHYSICAL REVIEW B **99**, 174433 (2019)

Temperature-dependent resistivity and anomalous Hall effect in NiMnSb from first principles

David Wagenknecht,[1,2,*] Libor Šmejkal,[3,4,1] Zdeněk Kašpar,[1,3] Jairo Sinova,[4,3] Tomáš Jungwirth,[3,5]
Josef Kudrnovský,[6] Karel Carva,[1] and Ilja Turek[2]
[1]*Charles University, Faculty of Mathematics and Physics, Ke Karlovu 3, CZ-121 16 Prague, Czech Republic*
[2]*Institute of Physics of Materials, Czech Academy of Sciences, Žižkova 22, CZ-616 62 Brno, Czech Republic*
[3]*Institute of Physics, Czech Academy of Sciences, Cukrovarnická 10, 162 53 Praha 6, Czech Republic*
[4]*Institut für Physik, Johannes Gutenberg Universität Mainz, D-55099 Mainz, Germany*
[5]*School of Physics and Astronomy, University of Nottingham, Nottingham NG7 2RD, United Kingdom*
[6]*Institute of Physics, Czech Academy of Sciences, Na Slovance 2, 182 21 Prague 8, Czech Republic*

(Received 15 March 2019; published 28 May 2019)

We present implementation of the alloy analogy model within fully relativistic density-functional theory with the coherent potential approximation for a treatment of nonzero temperatures. We calculate contributions of phonons and magnetic and chemical disorder to the temperature-dependent resistivity, anomalous Hall conductivity (AHC), and spin-resolved conductivity in ferromagnetic half-Heusler NiMnSb. Our electrical transport calculations with combined scattering effects agree well with experimental literature for Ni-rich NiMnSb with 1–2% Ni impurities on Mn sublattice. The calculated AHC is dominated by the Fermi surface term in the Kubo-Bastin formula. Moreover, the AHC as a function of longitudinal conductivity consists of two linear parts in the Ni-rich alloy, while it is nonmonotonic for Mn impurities. We obtain the spin polarization of the electrical current $P > 90\%$ at room temperature and we show that P may be tuned by chemical composition. The presented results demonstrate the applicability of an efficient first-principles scheme to calculate temperature dependence of linear transport coefficients in multisublattice bulk magnetic alloys.

DOI: 10.1103/PhysRevB.99.174433

I. INTRODUCTION

Microscopic description of finite temperature effects in magnetic materials represents a longstanding challenge for *ab initio* theory despite tremendous progress over the past 20 years in numerically demanding calculations of small quantities such as magnetocrystalline anisotropies or anisotropic magnetoresistance (AMR) [1–4]. A simulation of electrical transport coefficients at room temperature, that are important for spintronics, requires coupling of electrons to phonons or magnons.

One possibility of *ab initio* descriptions of electronic coupling to magnons and phonons is based on the alloy analogy model (AAM), which was recently employed to calculate electrical conductivity and the anomalous Hall conductivity (AHC) in elemental ferromagnets and binary alloys [5,6]. The AAM simulates the effect of phonons by transforming atomic displacements from the equilibrium positions to the multicomponent alloy. Also, spin fluctuations or the magnetic orientational disorder can be treated analogically in a similar way. The limiting case of full spin disorder is called the disordered local moment (DLM) state [7–10] and describes the paramagnetic state above the Curie temperature.

The AAM employing the coherent potential approximation (CPA) and Kubo-Bastin transport theory was implemented in the framework of the Korringa-Kohn-Rostoker method [5,6] while the supercell AAM within the Landauer-Büttiker scattering formalism was employed in the tight-binding linear muffin-tin orbital method (TB-LMTO) [11,12]. Both, the AAM-CPA and supercell AAM approaches allow one to also include on the same footing the substitutional or chemical disorder which is temperature independent. While the AAM-CPA is more efficient computationally, in particular in the presence of several types of defects with different concentrations, the supercell AAM can, at least in principle, e.g., describe correlated spin-fluctuations near the Curie temperature (the magnetic short-range order).

Recent zero-temperature calculations (with only static structural disorder) of electron transport within the TB-LMTO-CPA theory give good agreement with experimental data, e.g., for residual resistivity of partially ordered $L1_0$ FePt alloys [13], stoichiometric Heusler alloys [14], Mn-doped Bi_2Te_3 [15], antiferromagnetic (AFM) CuMnAs [16], for the sign of the AMR in NiMnSb [4], and the magnitude of the AMR in AFM Mn_2Au alloys [17]. Several of us have employed the relativistic variant of the TB-LMTO CPA-AAM to investigate an influence of high-temperature magnetic disorder on electrical resistivity in NiMnSb [18], the temperature-dependent electrical resistivity and the AHC in Ni a Ni-alloys [19], and the spin-resolved conductivities of the Cu-Ni alloys [20] at nonzero temperature; also justification of using the scalar-relativistic approximation for describing temperature-dependent electrical resistivity was demonstrated [21].

NiMnSb is a prototypical half-Heusler ferromagnet known for the presence of states only for one spin at the Fermi level

---

[*] Corresponding author: david@wagenknecht.email

[22,23] and its Curie temperature is as high as 730 K [24]. The measured value of the spin polarization of the electrical current is 45–58% [25–28] at low temperatures and about 50% at room temperature [29]; spin-polarized photoemission experiments show the spin polarization of the emitted electrons about 50% at 300 K [30]. The polarization of the ballistic transport for correlated electrons of about 50% was calculated for Au–NiMnSb–Au heterostructures by the SMEAGOL DFT code [31].

The TB-LMTO method (both LSDA and LSDA+U) was previously used to estimate the Curie temperature, exchange interactions, magnon spectra, and magnetic moments in $Ni_{2-x}MnSb$ alloys [32,33]. A saturation magnetization of NiMnSb is changing only slightly (by 5–10%) from zero to room temperature [26,34,35] and the magnetic moments were investigated by a polarized neutron diffraction [36]. Treating NiMnSb within LDA+U (for temperature $T = 0$) results only in a small correction to magnetic moments [33,37].

Here we apply our CPA-AAM for simulating the temperature dependence of conductivity, AHC, and spin-polarized conductivity of half-metal NiMnSb. In contrast to the so-far investigated materials using the AAM, NiMnSb is more complex and with a richer phenomenology due to two magnetic sublattices, a wide range of possible structure defects with similar formation energies [38] make it difficult to compare calculations and experiment, and Dresselhaus symmetry of its Wyckoff positions allow for spintronics effects such as the observed room-temperature spin-orbit torque in strained NiMnSb [4]. The material has been intensively studied for over 25 years, including AHC and electric resistance [24,25,36,39], which makes it a favorable system for testing *ab initio* methods.

II. FORMALISM

A. Structure model and electronic structure calculations

We employ an *ab initio* relativistic TB-LMTO method in combination with the multicomponent CPA and the atomic sphere approximation (ASA) [40]. The effect of temperature on the electronic structure is neglected in the DFT self-consistent electronic structure calculations, which turned out to be a good approximation for the temperature range from zero to room temperature. We simulate the effect of disorder via CPA-AAM in the transport calculations in conjunction with using the electronic structure determined at $T = 0$ K. Because of the displacement transformation of the TB-LMTO potential functions required by the AAM, the *spdf* − basis is used. We note that (standard) calculations without the displacements usually only employ the *spd* − basis, especially because of numerical expenses. The transformed potential functions must be expressed in a larger basis; therefore, functions for f−electrons are also included in our basis set.

NiMnSb has the cubic crystal structure $C1_b$ and the experimental lattice constant [24] $a_{\text{latt.}} = 5.927$ Å is used. Without chemical disorder, NiMnSb consists of four FCC sublattices Ni-Mn-empty-Sb equidistantly shifted along [111] direction. The empty sublattice denotes interstitial sites, i.e., empty positions in the half-Heusler lattice which would be occupied in the full-Heusler structure. We investigate Mn- and Ni-rich alloys with substitutional disorder, i.e., systems with sublattices $(Ni_{1-y}Mn_y)$-Mn-empty-Sb and Ni-$(Mn_{1-y}Ni_y)$-empty-Sb, respectively, with $y \in [0, 0.2]$. Notation $Ni_xMn_{2-x}Sb$ with x from 0.8 (Mn-rich) to 1.2 (Ni-rich) is used for brevity.

These defects are consistent with literature [4] and they have low formation energies [38]: 0.49 and 0.92 eV per formula unit for Mn- and Ni-rich case, respectively. Lower formation energies were obtained for Ni- and Mn-atoms occupying the interstitial crystallographic positions (0.20 eV and 0.73 eV per formula unit, respectively) but our calculated resistivity as a function of temperature significantly underestimates experimental values for these systems.

B. Lattice vibrations

The AAM of finite temperature effects was recently implemented within the TB-LMTO approach and applied to transition metals and simple alloys [19–21]. The model treats the vibrational effects by introducing for each single lattice site a mean-field CPA medium constructed from the chemically equivalent atoms but shifted in different spatial directions from their equilibrium position [5].

The displacements are chosen along high symmetry directions of the studied crystal. The shifts of atoms are realized via a linear transformation of the LMTO potential functions (with energy arguments omitted),

$$P^0 = D(\mathbf{u})\tilde{P}^0 D^T(\mathbf{u}), \tag{1}$$

where $\tilde{P}^0$ is the LMTO potential function of an atom at equilibrium position and the potential function P^0 corresponds to the atom displaced by the vector $\mathbf{u}$. The displacement vectors can be conveniently expressed in terms of displacement matrix $D_{L's',Ls}(\mathbf{u})$

$$D_{L's',Ls}(\mathbf{u}) = 8\pi\,\delta_{s's}\frac{(2\ell-1)!!}{(2\ell'-1)!!}\sum_{L''}\frac{(-1)^{\ell''}C_{LL'L''}}{(2\ell''-1)!!}J_{L''}(\mathbf{u})\,. \tag{2}$$

In Eq. (2), $C_{LL'L''} = \int Y_L(\hat{\mathbf{r}})Y_{L'}(\hat{\mathbf{r}})Y_{L''}(\hat{\mathbf{r}})\,d\Omega$ are the Gaunt coefficients with real spherical harmonics Y_L, J_L are regular solutions of the Laplace equation in the ASA [40], and the quantum number $L = (\ell, m)$ combining the orbital quantum number ℓ and the magnetic quantum number m is used [40], and s and s' are spin indices ($s, s' \in \{\uparrow, \downarrow\}$). The energy arguments and lattice-site indices are omitted for the sake of brevity. For the summation index in Eq. (2), a restriction $\ell = \ell' + \ell''$ holds; $D_{L's',Ls}(\mathbf{u}) = 0$ for $\ell' > \ell$ and $D_{L's',Ls}(\mathbf{u}) = \delta_{L's',Ls}$ for $\ell' = \ell$. After the transformation given by Eq. (1), the screened TB-LMTO potential functions P^α are obtained by using the matrix of screening constants α: $P^\alpha = P^0(1 - \alpha P^0)^{-1}$.

The increasing magnitudes of the displacements $\mathbf{u}$ correspond to the rising temperature according to the Debye formula. For N displaced atoms, the mean square displacement reads $\langle u^2\rangle = 1/N\sum_{i=1}^{N}|\mathbf{u}_i|^2$ and it is related to temperature T via the Debye approximation [41,42],

$$\langle u^2\rangle = \frac{9\hbar^2}{mk_B\Theta_D}\left(\frac{D_1(\Theta_D/T)}{\Theta_D/T} + \frac{1}{4}\right), \tag{3}$$

for atoms with identical masses m and the material-specific Debye temperature Θ_D. A standard notation for the reduced Planck constant $\hbar$ and the Boltzmann constant k_B is used and the Debye function is $D_n(x) = n/x^n \int_0^x t^n/(e^t - 1)\mathrm{d}t$. For simplicity, we omit the quantum zero-temperature fluctuations, i.e., the second term in Eq. (3). This omission is needed for vanishing of the calculated residual resistivity ($T = 0$) for ordered defect-free metallic systems [5]. Relative error in the temperature–displacement conversion coming from this neglect is about 15% at room temperature and 5% at 800 K, and corresponding relative errors in the electrical resistivity are about 27% and 10%, respectively.

C. Magnetic disorder

We investigate the influence of magnetic disorder on the electrical transport within a model of tilted local moments. The mean-field alloy was constructed by substituting a given site occupied by a single local moment oriented along the z direction by four different local moments tilted by the Euler angle θ from the z axis symmetrically in the four directions x, y, $-x$, and $-y$ and parametrized by the second Euler angle $\phi \in \{0.0\pi, 0.5\pi, 1.0\pi, 1.5\pi\}$. Four directions are sufficient for our case. This model is connected to temperature in the same way as in the previous high-temperature study [18], i.e., the interpolation of measured magnetization [34] is used and the reduced magnetization is identified with $\cos(\theta)$.

This approach interpolates between fully ordered spin ferromagnetic (FM) state ($T = 0$ K) and fully disordered spin state (DLM, T above the Curie temperature). Attempts to make descriptions of magnetic disorder more realistic were published [5,12,43]. However, a fully *ab initio* theoretical estimate of temperature-dependence of total magnetization $M_{\mathrm{tot}}(T)$ done by other authors can be also rather inaccurate because it employs the classical Boltzmann statistics (Monte Carlo) method, see the discussion in quaternary Heusler alloys [44].

We aim to estimate only the strength of the magnetic disorder contribution relative to the contribution from phonons and chemical disorder. The order of magnitude is determined from the energy difference between the disordered DLM state and the FM ground state, which amounts to $\Delta E \approx 12$ mRy (0.16 eV) per formula unit. In such approximation, room-temperature disorder roughly corresponds to $\theta = 0.10\pi$. A comparison to an experimentally observed change of the saturation magnetization [26,34,35] would give $\theta = 0.15\pi$. The use of experimental $M_{\mathrm{tot}}(T)$, if available, may be a better choice but, in general, an accurate relation of the tilting angle as a function of the temperature is missing.

D. Transport properties

The full conductivity tensor $\sigma_{\mu\nu}$ (μ and ν are Cartesian coordinates) is calculated by employing the Kubo-Bastin formula. It consists of $\sigma_{\mu\nu}^{(1)}$ and $\sigma_{\mu\nu}^{(2)}$ which in Ref. [45] are called the Fermi surface and the Fermi sea terms, respectively. The first one can be separated into the coherent part $\sigma_{\mu\nu}^{(1,\mathrm{coh})}$ and vertex corrections $\sigma_{\mu\nu}^{(1,\mathrm{v.c.})}$, see Ref. [46]. We note that the Fermi sea term contributes only to the antisymmetric part of the tensor $\sigma_{\mu\nu}$; the physical meaning is then related to the sum of $\sigma_{\mu\nu}^{(1,\mathrm{coh})}$ and $\sigma_{\mu\nu}^{(2)}$, see later Fig. 5.

The TB-LMTO method neglects electron motion inside the Wigner-Seitz cells, the velocity operators describe only intersite hopings [47], and the resulting effective velocity operators in a random alloy are spin-independent and nonrandom. The polarization of the spin-resolved currents,

$$P_{\mu\mu} = \frac{\sigma_{\mu\mu}^{(1,\mathrm{coh}),\uparrow} - \sigma_{\mu\mu}^{(1,\mathrm{coh}),\downarrow}}{\sigma_{\mu\mu}^{\mathrm{tot.}}}\,, \tag{4}$$

describes a quality of the spin-dependent transport [20,48] for the spin index $s = \uparrow$ and $s = \downarrow$. In the relativistic treatment of the transport, strictly speaking, one cannot define precisely the spin-resolved conductivities because of nonzero spin-flip contribution to the total conductivity (spin-nonconserving term)

$$\sigma_{\mu\nu}^{\mathrm{coh,flip}} = \sigma_{\mu\nu}^{(1,\mathrm{coh})} - \sum_{s=\uparrow,\downarrow} \sigma_{\mu\nu}^{(1,\mathrm{coh}),s}\,. \tag{5}$$

The spin-flip contribution was found to be small compared to the total conductivity, e.g., for the Cu-Ni alloy in a wide range of alloy compositions [20]. On the other hand, the spin-flip contribution is essential, e.g., for the Ni-rich NiFe alloys [49]. Calculating the coherent part of the conductivity tensor projected onto the spin-up and spin-down terms is a sufficient approximation for half-metals. The projected conductivity in Eq. (4) is then

$$\begin{aligned}\sigma_{\mu\nu}^{(1,\mathrm{coh}),s} = \sigma_0 \int_{-\infty}^{\infty} \mathrm{d}E\, f'(E)\, \mathrm{Tr}\{v_\mu \bar{g}_+^s(E) v_\nu [\bar{g}_+^s(E) \\ - \bar{g}_-^s(E)] - v_\mu[\bar{g}_+^s(E) - \bar{g}_-^s(E)] v_\nu \bar{g}_-^s(E)\}\,,\end{aligned} \tag{6}$$

where $\bar{g}_\pm^s(E)$, and v_μ is the averaged Green's function and velocity operator, respectively, expressed in an auxiliary form suitable for the numerical implementation within the relativistic TB-LMTO formalism after performing the configurational averaging. A real-energy variable is denoted E and $f'(E)$ is the energy derivative of the Fermi-Dirac distribution. To simplify the notation, $g_\pm(E) = g(E \pm i0)$ is used. In Eq. (6), $\sigma_0 = e^2/(4\pi V_0 N_0)$ depends on the charge of the electron e, on the volume of the primitive cell V_0, and on the number of cells N_0 in a large finite crystal with periodic boundary conditions. If there was no spin-orbit interaction, in the two-current model [50], the sum $\sigma_{\mu\nu}^{(1,\mathrm{coh}),\uparrow} + \sigma_{\mu\nu}^{(1,\mathrm{coh}),\downarrow}$ would correspond to the total coherent conductivity.

For an ideal half-metal (with exactly one of the spin-channels insulating), this projection is valid and $P \to 1$ (equals one without the spin-orbit interaction). If both channels are identical, e.g., for nonmagnetic materials, $P = 0$.

The effect of finite temperature is treated within the AAM. Thus the configurationally averaged quantities $\bar{g}_\pm^s(E)$ are calculated not only by averaging over the different alloy configurations, but also over distinctly displaced (or magnetization tilted) configurations. The contribution from the Fermi-Dirac distribution can usually be neglected as we checked for several transition metals (Pt, Pd, Fe, Ni). Thus we will use the zero-temperature limits of the conductivity formulas CPA configurationally averaged over the alloy and displacement configurations.

E. Computational details

The mesh of $150 \times 150 \times 150$ k-points in the Brillouin zone was used for transport calculations if not specified otherwise. Smaller numbers of k-points as for, e.g., pure metals, are required because of a large self-energy term originating from chemical or temperature disorder. Increasing the mesh to 200^3 k-points leads to a correction of 0.05 % for the isotropic resistivity.

In previous reports, the Debye temperature was theoretically estimated to be between 250 and 300 K [39], measured (312 ± 5) K [51] or 322 K [52], and calculated 327 K [53] and 270 K [54]. We used $\Theta_D = 320$ K (see later Fig. 4); the above scatter in Debye temperature values leads to approx. 10% error in the root-mean-square displacement $\sqrt{\langle u^2 \rangle}$. The best agreement between experimental data [25,39,55] as concerns the slope of the calculated temperature dependence of the resistivity is obtained for $\Theta_D = 350$ K and 2% Ni-rich NiMnSb.

The Debye theory was derived for systems of identical atoms; for alloys and compounds, magnitudes of the atomic displacements might be different for different species [56]. To get a rough estimation of sensitivity of the transport properties to the displacement magnitudes, we investigated (a) the magnitudes identical for each atom or (b) scaled according to atomic masses [57]. In our case, for atomic masses, $m(\mathrm{Ni}) : m(\mathrm{Mn}) : m(\mathrm{Sb}) \approx 1 : 0.93 : 2.07$ holds. The TB-LMTO approach assumes empty spheres at the empty positions in the half-Heusler lattice which would be occupied in the full-Heusler lattice. The potential functions of the empty sphere may be (i) formally displaced like other nuclei or (ii) independent on atomic shifts. We have tested all four possibilities, i.e., combinations of models (a) and (b), and (i) and (ii) above. We have found deviations in the isotropic resistivities of the order of 5% by assuming $\sqrt{\langle u^2 \rangle} = 0.20\, a_\mathrm{B}$ and $0.25\, a_\mathrm{B}$, where a_B is the Bohr radius. This value should be considered as a systematic error of the AAM (later shown by error bars in Fig. 4). In the following sections, identical magnitudes of the displacements are assumed for all atoms. Each atom was assumed to have eight different directions of displacements (within the CPA) uniformly distributed around its equilibrium position.

III. RESULTS

A. Calculated magnetic moments and density of states

The magnetic moment of the stoichiometric NiMnSb is $m = 4.0\mu_B$ per formula unit, which agrees well with the half-metallic character (the Fermi level in the minority gap), with its integer number of electrons per formula unit and it is in good agreement with experimental data [36] and previous calculations [4,37]. In Fig. 1, we show the average moment, local magnetic moments, as well as local Mn- and Ni-impurity magnetic moments on Ni and Mn sublattices, respectively. Local moments for the stoichiometric system are $m_\mathrm{Ni} = 0.26\mu_B$, $m_\mathrm{Mn} = 3.75\mu_B$, $m_\mathrm{Sb} = -0.05\mu_B$, and $m_\mathrm{empty} = 0.08\mu_B$; for 10% Ni-rich $m_\mathrm{Ni} = 0.20\mu_B$, $m_\mathrm{Mn} = 3.69\mu_B$, $m_\mathrm{Sb} = -0.07\mu_B$, $m_\mathrm{empty} = 0.06\mu_B$, and $m_\mathrm{impurity} = -0.64\mu_B$; and for 10% Mn-rich $m_\mathrm{Ni} = 0.24\mu_B$, $m_\mathrm{Mn} = 3.68\mu_B$, $m_\mathrm{Sb} = -0.05\mu_B$, $m_\mathrm{empty} = 0.08\mu_B$, and $m_\mathrm{impurity} = -1.88\mu_B$ (the m_empty denotes moment induced on empty spheres at the interstitial positions). Both the Mn and Ni impurities tend to couple antiferromagnetically and thus decrease the net moment with increasing disorder; however, the main reason is slightly different for the Mn- and Ni-rich systems: In the former one, Mn atoms on the Ni sublattice have opposite directions of the magnetic moments with respect to Mn atoms on their own sublattice and the sum of all the moments decreases with increasing concentration of antiparallel Mn moments. For the Ni-rich case, the concentration of Mn atoms having large moment decreases and they are replaced by Ni having moments much smaller (five to thirty times, see Fig. 1); moreover, with the antiparallel orientation.

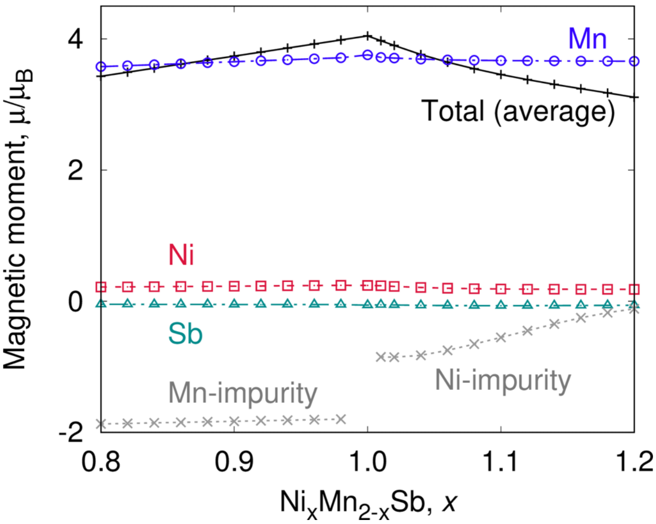

FIG. 1. Total averaged magnetic moment (per formula unit) of Ni- and Mn-rich NiMnSb and spin magnetic moments of individual atoms for zero temperature. The Ni/Mn-impurity data set presents the local magnetic moments of Ni and Mn atoms placed on the crystallographic position of the second atom.

The spin-resolved density of states (DOS) of the studied systems is displayed in Fig. 2. The stoichiometric NiMnSb is the half-metal as indicated by the DOS in Fig. 2(b). Our results are in agreement with literature [37]. The influence of atomic displacements slightly broadens peaks in the DOS (see Fig. 2 for 540 K) but the DOS around the Fermi level is almost the same. The half-metallic character is thus preserved even at nonzero temperatures.

The behavior of Ni-rich and Mn-rich samples differs significantly. Mn atoms on Ni sublattice preserve the half-metallic character of the alloy, see Fig. 2(a), while Ni atoms on the Mn sublattice give a nonzero spin-down DOS at the Fermi level for Ni concentration $x \gtrsim 1.02$, see Figs. 2(d) and 3. This opens the spin-down channel for the electron transport, which in turn leads to an increase of the conductivity with increasing Ni impurity content (for $x \gtrsim 1.07$), see Fig. 6(a) and also Fig. 11 in the Appendix. Later presented electrical transport calculations are in agreement with these changes. The inset [Fig. 2(c)] shows a minor influence of the magnetic disorder (tilting of moments with $\theta = 0.1\pi$) on the DOS of stoichiometric NiMnSb at both zero and finite temperature ($T \approx 220$ K).

Figure 3 presents the DOS at the Fermi level for the Ni-rich NiMnSb. The negligible DOS in the minority channel is

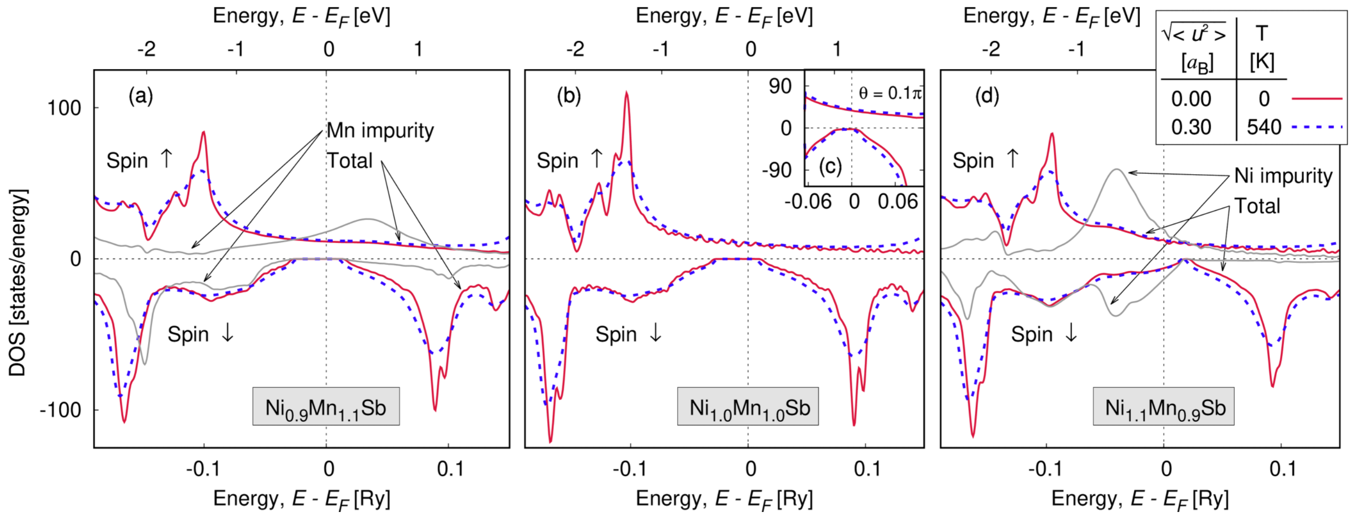

FIG. 2. Temperature and alloying disorder dependence of the half-metallicity in NiMnSb. Atomic concentrations are used as weights of the local DOS and data for impurities (Mn and Ni). (a) The 10% Mn-rich NiMnSb preserves the half-metallic character for all of the considered atomic displacements. Mn-impurity virtual bound state forms in the majority spin-channel. (b) Stoichiometric NiMnSb exhibits the half-metallic band gap also at room temperature. Inset (c) shows that magnetic disorder (tilted magnetic moments with $\theta = 0.1\pi$) has almost no influence on DOS, especially in the minority channel. (d) The 10% Ni-rich NiMnSb is no longer half metal and the states around E_F are almost independent on temperature.

preserved for small amounts (up to 2%) of Ni impurities. With increasing Ni concentration, the difference between spin-up and spin-down DOS is getting smaller. They become equal at approximately 11% of impurities and the spin-down states are dominant after this value.

For further investigation of the electronic structure in the terms of the Bloch spectral function, see Appendix C which shows smeared bands for the Ni-rich NiMnSb.

B. Temperature-dependent resistivity and anomalous Hall effect calculation

Calculated temperature dependence of the resistivity and the anomalous Hall effect (resistivity ρ_{xy}) are shown in Fig. 4.

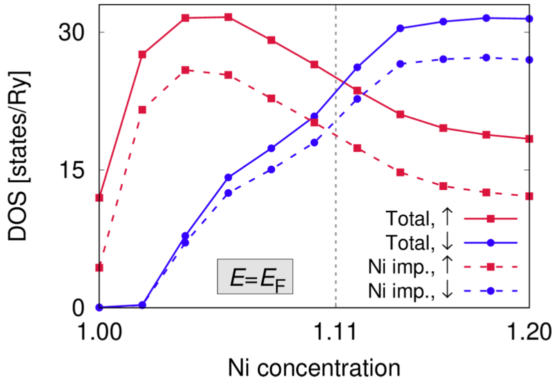

FIG. 3. Total DOS at the Fermi level (solid lines) as well as the local DOS for Ni impurities (dashed lines) are increasing with higher substitution of Mn atoms by Ni. The spin-up states (red lines, squares) are dominant for less than 10% of Ni impurities, after 12% the spin-down states (blue lines, circles) prevail. The total DOS (sum of the spin channels, not shown here) increases monotonically.

The results are in agreement with experimental data; measured resistivities are taken from Refs. [39,55], and experimental ρ_{xy} was obtained by combining Refs. [24,55].

Experimentally observed resistivity of NiMnSb exhibits a linear dependence on temperature [39,55] (up to room temperature) which was ascribed to phonons [24]. The resistivity calculated only with phonons and impurities (without magnetic disorder) also leads to an almost linear dependence for temperatures from 100 K to 300 K and our data agree with measured values [39,55]. This agreement indicates that phonons can be considered as the most important scattering mechanism in this temperature range. The quadratic (nonlinear) behavior of calculated electrical resistivities as a function of temperature is important especially for low temperatures ($T \lesssim 100\,\mathrm{K}$) and experimental resistivities exhibit only a small deviation from the quadratic form [34]. The residual resistivity and the weak influence of magnons are in agreement with other studies [4,24,39,55]. It is consistent with the high Curie temperature, resulting in a weak influence of magnetic disorder and it also agrees with the DOS showing a negligible influence of the magnetic disorder on the number of carriers at the Fermi level [Fig. 2(c)]. Our results also agree with the observed sign of the AMR [4] and its qualitatively good description is also given by the finite-relaxation time (FRT) approximation, see Appendix B.

The comparison of calculated and measured ρ and ρ_{xy} indicates that the presence of the Mn-rich phase in real samples is unlikely because an increasing presence of additional Mn atoms dramatically increases both the resistivity and ρ_{xy} at the zero temperature and, moreover, slopes of these quantities as a function of temperature are much higher than the measured counterparts [24,36], see Fig. 4. The calculated transport properties as a function of Ni impurity are nonmonotonic, both the resistivity and ρ_{xy} have maxima around a 10% Ni-rich sample. The measured residual resistivity could correspond to

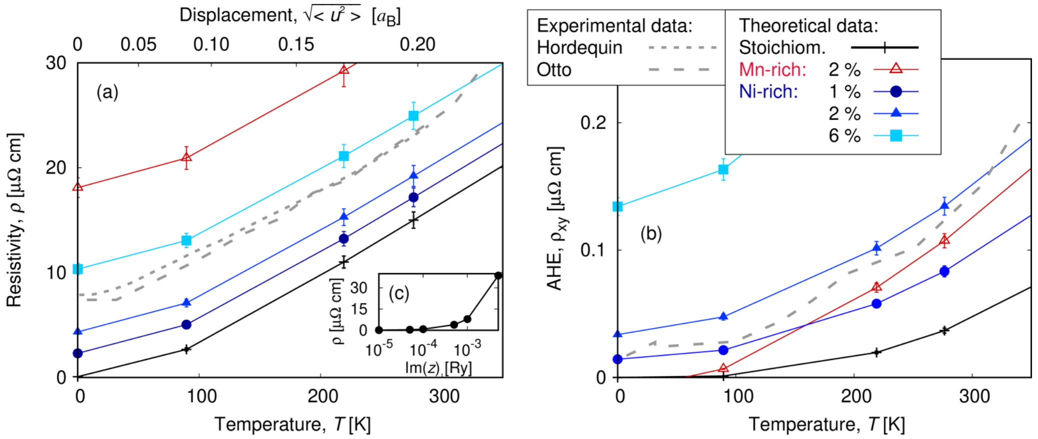

FIG. 4. (a) The isotropic resistivity and (b) anomalous Hall effect (ρ_{xy}) of Ni- and Mn- rich NiMnSb monotonously increase with increasing temperature. Experimental results [24,39,55] agree with our theoretical data obtained for the Ni-rich case with low concentration of impurities. (c) The model of finite-relaxation time (stoichiometric NiMnSb) for an unknown disorder qualitatively agrees with calculated data at nonzero temperature.

a presence of additional Ni atoms on the empty atomic sites (unoccupied positions of the half-Heusler structure); however, the calculated results contradict the experimental data that exhibit much steeper temperature dependence of both the resistivity and the ρ_{xy} for these defects.

Comparing our theoretical results with data from literature (especially Refs. [24,55]), the best mutual agreement is obtained for Ni-rich samples with 1–2% of Mn atoms replaced by Ni; we note that the exact composition and chemical disorder in the experimental samples is unknown. In real samples, a wide range of different defects may occur but a systematic investigation of the huge number of different combinations of such defects goes beyond the scope of this paper.

In calculations including the magnetic disorder that corresponds to room temperature, transport properties differ less than by 1% when only Mn moments are tilted or when moments of all atoms are tilted. It is caused by a dominant contribution to the total moment from Mn atoms. The influence of magnetic disorder on the electrical resistivity for the stoichiometric NiMnSb is negligible up to room temperature as can be seen in Table I. Experimentally documented decrease of the saturation magnetization is from $4.0\mu_B$ at zero temperature to $3.6\mu_B$ at room temperature [26,34,35]. When we assume magnetic disorder corresponding to the same change of magnetization, $\theta = 0.14\pi$, we obtain electrical resistivity between $\rho = 17\,\mu\Omega\,\mathrm{cm}$ and $\rho = 25\,\mu\Omega\,\mathrm{cm}$ (see the caption of Table I). It is in perfect agreement with experimental values of $\rho = 23\,\mu\Omega\,\mathrm{cm}$. The small influence of magnetic disorder on electrical transport properties agrees with literature [55] and it is supported by negligible influence on the DOS at the Fermi level, see the inset in Fig. 2 for $\theta = 0.1\pi$.

The calculated weak dependence of the resistivity on magnetic disorder justifies neglecting magnetic disorder in further discussion for $T \lesssim 300\,\mathrm{K}$. However, the larger magnetic disorder (for larger temperatures) dramatically decreases the total magnetic moment and increases the resistivity value, see Table I.

Chemical impurities decrease the total magnetic moment, similar to the pure magnetic disorder. If the scattering properties are considered as a function of the alloy magnetization, results obtained by the different scattering mechanisms (magnetic disorder and chemical impurities) quantitatively agree with each other.

C. Anomalous Hall effect mechanism in NiMnSb

We calculated the $\sigma_{xy}^{(1)}$ and $\sigma_{xy}^{(2)}$ contributions to the anomalous Hall effect at zero temperature. In Fig. 5, we show the separation of the AHC into $\sigma_{xy}^{(1)}$ and $\sigma_{xy}^{(2)}$ contributions; for a detailed analysis of the contributions see Appendix A. We observe a strong dependence of the AHC magnitude on the type of disorder. In general, the AHC is much larger for the Ni-rich system ($\sigma_{xy} \sim 10^3\,\mathrm{S/cm}$) than for the Mn-rich NiMnSb ($\sigma_{xy} \sim 10^1\,\mathrm{S/cm}$). Both the Mn and Ni rich cases show the same positive sign of the AHC in agreement with experimental literature [4,39,55]; an exception of a small negative AHC is found for the 2% Mn-rich material due to large negative vertex corrections. The vertex part of the AHC diverges in the dilute limit, approaching zero disorder, of both Ni- and Mn-rich branches. Similar behavior is obtained in binary transition-metal alloys due to the skew-scattering

TABLE I. Pure NiMnSb: Isotropic resistivity (in $\mu\Omega\,\mathrm{cm}$, seven rows and three columns in the right bottom block of the table) for different magnitudes of displacements ($\sqrt{\langle u^2\rangle}$) and tilting angles ($\theta$). Empty values in the table were smaller than the numerical accuracy. Room temperature roughly corresponds to $\sqrt{\langle u^2\rangle} \approx 0.21\,a_\mathrm{B}$ for $\Theta_D = 300\,\mathrm{K}$ (between the two bold values), and the experimental decrease of saturation magnetization is up to 10% [26,34,35].

Tilting angle, θ	Total mag. moment	Displacement, $\sqrt{\langle u^2\rangle}$ 0.00 a_B	0.20 a_B	0.25 a_B
0.00π	$4.04\,\mu_B$	-	15.0	23.4
0.10π	$3.82\,\mu_B$	0.47	15.6	24.0
0.14π	$3.58\,\mu_B$	1.38	**16.7**	**25.2**
0.20π	$3.16\mu_B$	6.47	22.4	31.8
0.30π	$2.25\mu_B$	42.5	59.3	68.3
0.40π	$1.17\mu_B$	120	133	140
0.50π	$0.00\mu_B$	173	180	184

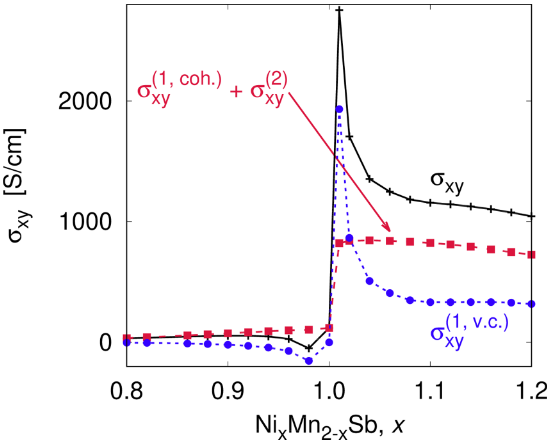

FIG. 5. Negative sign of the calculated ($T = 0$) total AHC σ_{xy} (black solid line) was observed only for $Ni_{0.98}Mn_{1.02}Sb$, which is caused by a small contribution of the intrinsic term (red dashed line with squares) but dominant vertex corrections (blue dashed line with circles).

mechanism [58]. The small magnitude of the Fermi sea term allows us to neglect the $\sigma^{(2)}$ term in the temperature study of the AHC by the AAM, which substantially speeds up our calculations.

Simulating up to 20% of Mn or Ni-rich swapping disorder allows us to vary in our calculations the residual resistivities over a broad range from $\rho \approx 0$ for stoichiometric NiMnSb to 150 $\mu\Omega$ cm for 20% of Mn-rich and 11 $\mu\Omega$ cm for 10% Ni-rich materials. In Fig. 6(a), we show the dependence of the longitudinal resistivity on the disorder. While the resistivity monotonically increases for the Mn-rich system, consistent with the appearance of the virtual bound state [Fig. 2(a)], for the Ni-rich case we observe a maximum around 10% of Ni.

In Figs. 6(b) and 6(d), we present the anomalous Hall versus longitudinal conductivity dependence for both the Mn-rich and Ni-rich calculations. A linear fit of the dependences is shown in Figs. 6(b) and 6(d). In the insets [Figs. 6(c) and 6(e)], we also show the experimentally relevant anomalous Hall angle ρ_{xy}/ρ_{xx} obtained by the full inversion of the conductivity tensors (instead of the usually used approximation $\rho_{xy} \sim \sigma_{xy}/\sigma_{xx}^2$). A part of the Ni-rich branch belongs to a rather high conductivity regime (10^5 S/cm) and follows linear dependence $\sigma_{xy} \sim \sigma_{xx}$, signaling the dominating extrinsic, skew-scattering mechanism of the AHC [59,60]. In contrast, the behavior of Mn-rich system with higher conductivities is nonmonotonic but different from a power dependence reported in literature [60]. It is rather linear for larger conductivities (small Mn disorder below 6%), where the AHC is influenced by the disorder [59], see Fig. 6(d).

Interestingly, for Ni-rich branch around ∼10 %, the slope of the AHC as a function of σ_{xx} changes sign. It signals multiband character of the transport [Fig. 6(b)], see also Appendix C. As long as the Friedel sum rule [60,61] can be applied, the change of the AHC sign can be attributed to the change of the dominating spin channel at the concentration of ∼10 % Ni-rich (Fig. 3).

We note that the half-metal and multiband character of the transport in NiMnSb can be responsible for notably different behavior than that generally reported in metals. For metals, only one slope exists (variations of disorder are typical on the level of a few percents) and it is difficult to achieve more than one conductivity regime [59,60].

D. Spin-resolved electrical conductivities

To obtain maximal efficiency of the spin-polarized currents, their polarization P should approach unity and both the spin-flip part (of the coherent conductivity) and the vertex part (of the total conductivity) should be negligible. Ni-rich NiMnSb has ten or more times larger conductivity of the majority channel than similar concentration of the Mn-rich material and, unlike the minority channel, it strongly depends on temperature (especially Ni-rich), see Appendix D.

The Mn impurities do not destroy the half-metallic character of the system while the Ni impurities lead to nonzero density of minority carriers at the Fermi level (Fig. 2). It leads to the spin polarization that is almost unity for the Mn-rich case (for all temperatures) and in the Ni-rich region

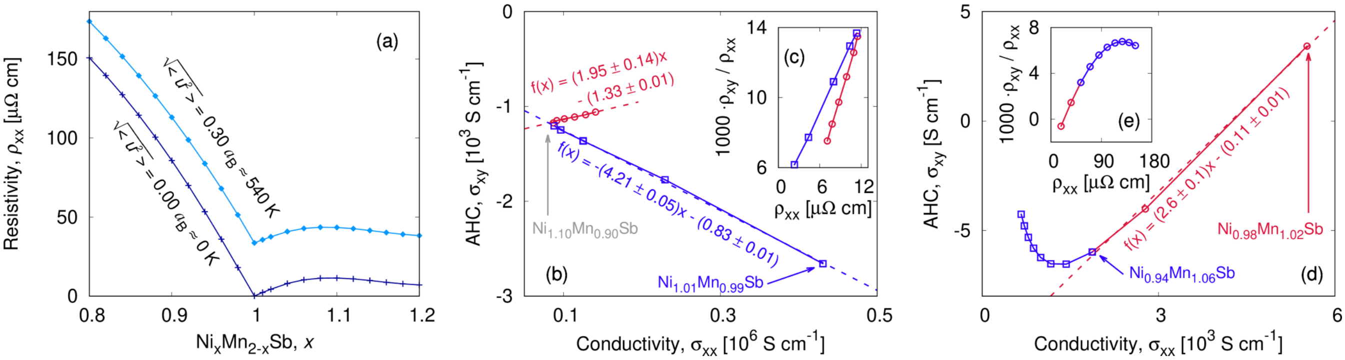

FIG. 6. Total resistivity (a) for zero and finite (540 K) temperature is monotonic in the Mn-rich region but it has a maximum in the Ni-rich case at 10% and 8% of Ni impurities for $T = 0$ and 540 K, respectively. Zero-temperature AHC plotted as a function of the total conductivity has (b) two piecewise linear parts for the Ni-rich NiMnSb, one having a negative slope (fitted from 1, 2, 4, 6, 8, and 10% of Ni) and the second with a positive slope (10, 12, 14, 16, 18, and 20% of Ni). The parts are distinguishable when the resistivity for the same data is plotted (c). The same dependence in the Mn-rich region (d) exhibits a linear (2, 4, and 6% of Mn impurities) and a nonmonotonic (8, 10, 12, 14, 16, 18, and 20% of Mn) behavior; a ratio of resistivities (e) shows a smooth transition between both parts.

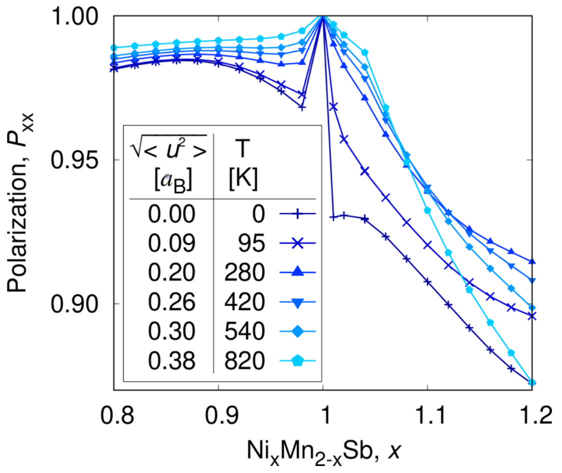

FIG. 7. The spin-polarization of the electrical current for the in-plane direction is almost unity for the Mn-rich NiMnSb (small total conductivity) and it is predicted to be larger than 90% also in the Ni-rich system at room temperature.

it decreases with increasing impurity concentration or increasing temperature, see Fig. 7. However, even at room temperature and in the Ni-rich case, $P > 0.9$, which ensures highly polarized electrical current. The influence of the spin-flip term and vertex contributions on the polarization P is small, see Appendix D, which justifies employing Eq. (4).

Combined effects of magnetic and atomic displacements were investigated for stoichiometric NiMnSb. The change between $T = 0$ and room temperature ($\sqrt{\langle u^2 \rangle} = 0.21\, a_{\mathrm{B}}, \theta = 0.1\pi$) is 0.8% in the polarization value P.

We focused on systems similar to samples from literature (about 1 to 2% Ni-rich, see Sec. III B) but experimental $P(T)$ was measured with a wide range of samples: 44% for a free surface of a bulk material with $M_S = 3.6\mu_B$ [28], 45% for a thin film with $M_S = 4.0\mu_B$ [25], 45% for bulk NiMnSb with $M_S = 3.6\mu_B$ [26], 58% for thin films [27], and from 20–50%, depending on temperature in polycrystalline samples [30]. Saturation magnetization $M_S < 4.0\mu_B$ indicated disordered samples but the disorder is unknown, which makes it hard to reproduce. The discrepancy is not caused by the magnetic disorder [18]. It is dominant close to the Curie temperature, where spin fluctuations lead to $P = 0$; the zero polarization cannot be achieved by phonons themselves. For room temperature, the decrease of the polarization caused by the magnetic disorder is negligible, i.e., $P > 0.98$ for $\theta \approx 0.14\pi$.

We also investigated the polarization anisotropy. Similarly, the small AMR (difference between σ_{zz} and $\sigma_{xx} = \sigma_{yy}$ is around 0.25%), the polarization P_{zz} is almost the same as $P_{xx} = P_{yy}$.

The polarization for Mn- and Ni-rich cases with impurities occupying the empty crystallographic position of the Heusler structure was also calculated. The Ni atoms on interstitial positions behave similarly to the Ni-rich system with Mn atoms substituted by Ni impurities; on the other hand, for the 20% Mn-rich case with access Mn in the interstitial positions, $P(0\ \mathrm{K}) \approx 91\,\%$ and $P(400\ \mathrm{K}) \approx 87\,\%$. This demonstrates a strong dependence of the polarization on the kind of chemical disorder.

IV. CONCLUSIONS

We have formulated the CPA-AAM approach in the framework of the fully relativistic TB-LMTO method and Kubo-Bastin formula for the calculation of the longitudinal and anomalous Hall conductivities and applied it to the half Heusler FM NiMnSb with alloy and temperature-induced disorder. The main conclusions are (i) The calculated temperature dependence of the longitudinal conductivity is dominated by the phonon contribution and it is in agreement with experimental literature. Specifically, the Ni-rich alloys (from 1–2% of Ni atoms on the Mn sublattice) fit the experimental data [24,55]. (ii) The Ni-rich samples are also consistent with the sign of the AMR found in literature. (iii) The effect of the Fermi-sea contribution to the AHC is generally weak although it is stronger for the Mn-rich case. The anomalous Hall effect in Ni-rich NiMnSb is dominated by the $\sigma^{(1)}$ part ("integration

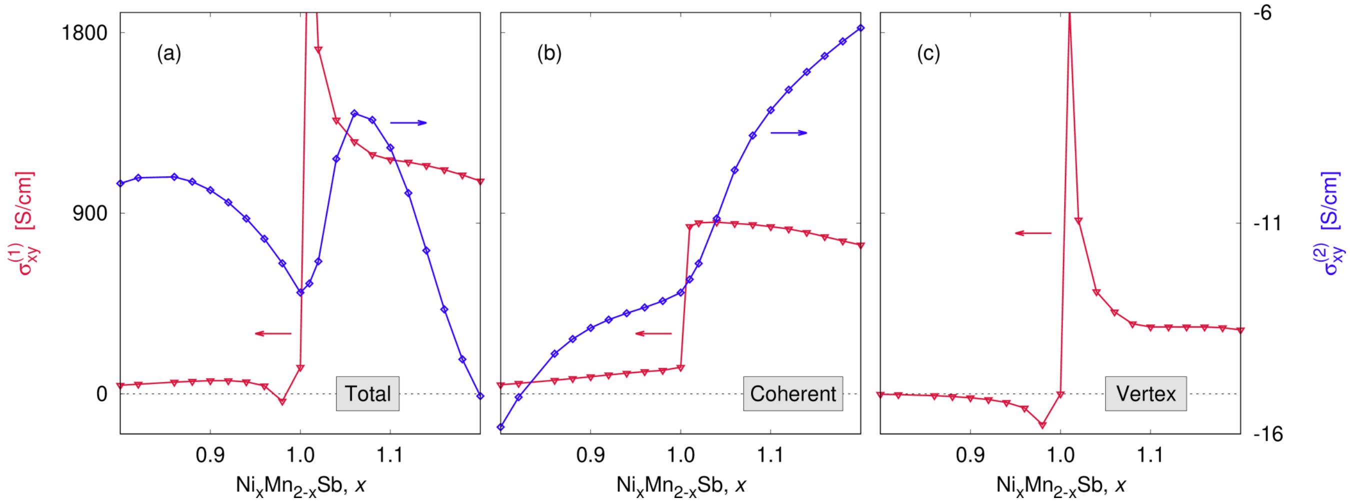

FIG. 8. $\sigma_{\mu\nu}^{(1)}$ (left axes, red lines with triangles) and $\sigma_{\mu\nu}^{(2)}$ (right axes, blue lines with squares) contribution to the anomalous Hall effect in NiMnSb: (a) Total conductivity, (b) its coherent part, and (c) the vertex contribution to $\sigma_{xy}^{(1)}$.

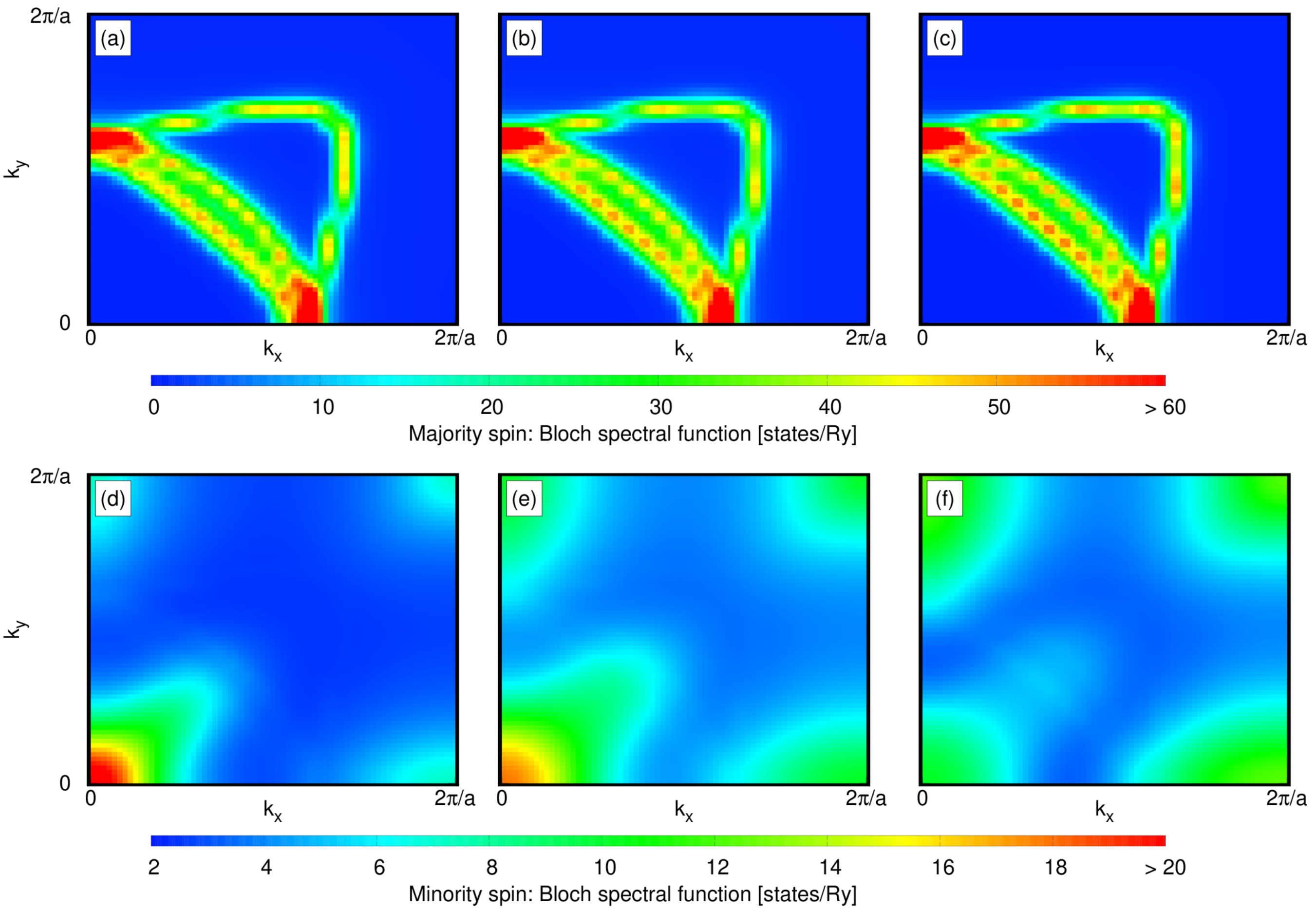

FIG. 9. Bloch spectral functions displayed for the Fermi level and $k_z = 0$ for the majority spin (a), (b), and (c) and the minority one (d), (e), and (f); (a) and (d) for $Ni_{1.06}Mn_{0.94}Sb$, (b) and (e) for $Ni_{1.10}Mn_{0.90}Sb$, and (c) and (f) for $Ni_{1.14}Mn_{0.86}Sb$.

over the Fermi sheets") of the conductivity, while for the Mn-rich case, the $\sigma^{(2)}$ ("complex integration over the valence spectrum") term represents a sizable contribution of the order of 20%. Moreover, qualitatively different behavior of the AHC was observed for the Mn- and Ni-rich systems. (iv) The calculated spin-current polarization is typically greater than 0.9 for studied concentrations of the impurities and its behavior correlates with the half-metallic-like character (small amount of states in the minority channel). Its values overestimate available experimental data. (v) The calculations indicate the possibility to influence current spin polarization by tuning chemical composition.

ACKNOWLEDGMENTS

D.W., J.K., K.C., and I.T. acknowledge the support of the Czech Science Foundation (Grant No. 18-07172S). L.Š., J.S., and T.J. acknowledge support from the Alexander von Humboldt Foundation, the Transregional Collaborative Research Center (SFB/TRR) 173 SPIN+X, EU FET Open RIA (Grant No. 766566), and the Czech Science Foundation (Grant No. 19-28375X). Z.K. acknowledges support from the Ministry of Education of the Czech Republic (Grant No. LM2015087 and LNSM-LNSpin).

This work was supported by the Ministry of Education, Youth and Sports from the Large Infrastructures for Research, Experimental Development and Innovations project IT4Innovations National Supercomputing Center—LM2015070. Access to computing and storage facilities owned by parties and projects contributing to the National Grid Infrastructure MetaCentrum provided under the program Projects of Large Research, Development, and Innovations Infrastructures (CESNET LM2015042) is greatly appreciated.

APPENDIX A: CONTRIBUTIONS TO THE ANOMALOUS HALL CONDUCTIVITY

We study an influence of different contributions to the AHC, see Sec. II D. Its total value (Fig. 5 for $T = 0$) is given by the $\sigma_{xy}^{(1)}$ and $\sigma_{xy}^{(2)}$ terms. The major contribution comes from the former one, which is about two orders of magnitude larger than $\sigma_{xy}^{(2)}$, see Fig. 8. This justifies omitting $\sigma_{xy}^{(2)}$ in the temperature-dependent calculations. While the concentration dependence of $\sigma_{xy}^{(1,\mathrm{coh})}$ consists of two linear parts (one in the Mn-rich region, the second one for the Ni-rich system), $\sigma_{xy}^{(1,\mathrm{v.c.})}$ diverges for small concentrations of impurities.

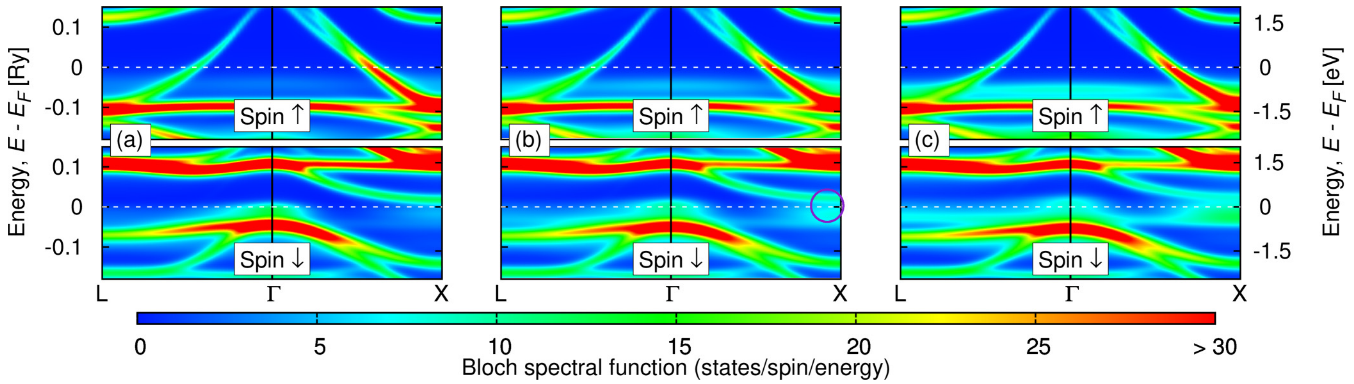

FIG. 10. Bloch spectral functions of (a) $Ni_{1.06}Mn_{0.94}Sb$, (b) $Ni_{1.10}Mn_{0.90}Sb$, and (c) $Ni_{1.14}Mn_{0.86}Sb$ for spin-up (upper panels) and spin-down (lower panels) channels.

APPENDIX B: FINITE-RELAXATION TIME MODEL AND THE ANISOTROPIC MAGNETORESISTANCE

The FRT model corresponds to the spin- and orbital independent scatterings, which is technically realized by adding a finite imaginary constant (Im z) to the Fermi energy in corresponding Green functions in the Kubo-Bastin equation. The FRT model assumes zero vertex corrections and does not allow us to separate out the phonon and spin-disorder contributions to the conductivity tensor. The calculated negative AMR sign for Hall bars oriented along the [110] directions within the FRT is consistent with previous estimates of AMR in NiMnSb [4], i.e., $\rho(\mathbf{m} \parallel \mathbf{j}) < \rho(\mathbf{m} \perp \mathbf{j})$, where ρ is the longitudinal resistivity and $\mathbf{j}$ the electric current. Remarkably, the AMR value is well described within the FRT applied in combination of the 10% Ni-rich disorder. Our calculated value changes from $(\rho_{\mathbf{m}\parallel E[110]} - \rho_{\mathbf{m}\perp E[110]})/(\rho_{\mathbf{m}\parallel E[110]} + \rho_{\mathbf{m}\perp E[110]}) = -1.6\%$ (for Im $z = 10^{-5}$ Ry corresponding to low temperatures) to $-0.3\,\%$ (roughly to room temperature residual resistivity values, Im $z = 3 \times 10^{-3}$ Ry). The sign of the AMR is the same as in Mn-doped GaAs and opposite to the typical transition metal ferromagnets Ni, Co, and Fe.

APPENDIX C: BLOCH SPECTRAL FUNCTIONS

In this Appendix, the electronic structure is visualized by using the spin-resolved Bloch spectral functions [40]

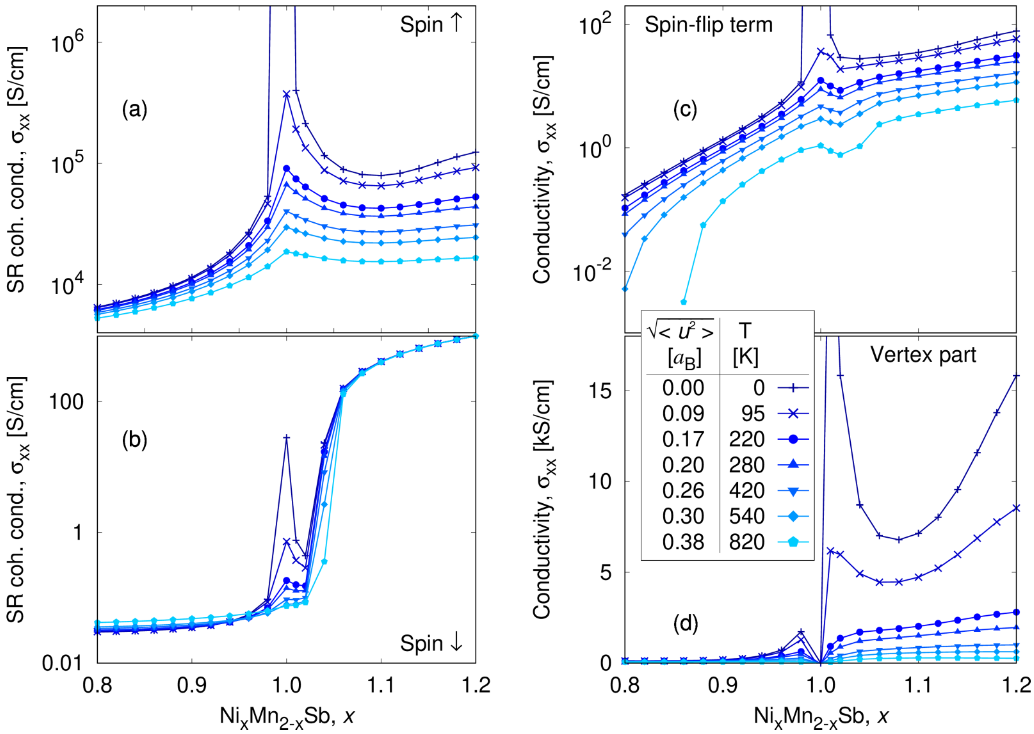

FIG. 11. The spin-resolved in-plane (perpendicular to the magnetization) coherent conductivity for the majority channel (a) differs by several orders of magnitude for the Mn- and Ni-rich cases. On the other hand, the conductivity for the minority channel (b) is almost independent of the temperature, except for extreme displacements in the Mn-rich case. Both the spin-flip term (c) and vertex part of the conductivity (d) are larger for the Ni-rich system than in the Mn-rich region.

$\mathcal{A}^s(\mathbf{k}, E)$, where $s \in \{\uparrow, \downarrow\}$ is the spin index, **k** is a reciprocal-space vector, and E is the electron energy. For 6, 10, and 14% of Ni-rich NiMnSb, we plot in Fig. 9 the Bloch spectral function for $E = E_F$ and in Fig. 10 the energy-dependent spin-resolved Bloch spectral function along the $L - \Gamma - X$ path in the reciprocal space.

We observe that at 10% of Ni impurities in the Ni-rich system minority-spin bands smeared due to disorder emerge at the Fermi surface (region marked by the violet circle in Fig. 10(b)), also visible for 14%, but absent for 6%. These bands may be responsible for the AHC slope change, Fig. 6, where we observe smearing out of the spin-down band at the Γ point and emergence of more spectral weights at around the X point for the critical Ni disorder. See also Fig. 9 for $k_z = 0$ and total DOS at the Fermi level in Fig. 3.

APPENDIX D: SPIN-RESOLVED TRANSPORT QUANTITIES

The spin-resolved conductivity is crucial for spintronic applications but its measurement is difficult. The total conductivity is the largest (infinitely high) for stoichiometric NiMnSb with resistivity going to zero.

For most of the impurities and temperatures, the conductivity of the majority spin channel is at least two orders of magnitude larger than the vertex contribution and about four orders of magnitude larger than the spin-flip term (Fig. 11). The spin-flip term [Fig. 11(c)] and the vertex contributions [Fig. 11(d)] are at least three orders of magnitude smaller than the conductivity of the majority channel. These features justify the simple definition of the spin polarization of the current in terms of the coherent majority and minority conductivities in Eq. (4).

[1] R. O. Jones, Rev. Mod. Phys. **87**, 897 (2015).

[2] G. Kotliar, S. Y. Savrasov, K. Haule, V. S. Oudovenko, O. Parcollet, and C. A. Marianetti, Rev. Mod. Phys. **78**, 865 (2006).

[3] J. Bass, J. Magn. Magn. Mater. **408**, 244 (2016).

[4] C. Ciccarelli, L. Anderson, V. Tshitoyan, A. J. Ferguson, F. Gerhard, C. Gould, L. W. Molenkamp, J. Gayles, J. Železný, L. Šmejkal, Z. S. Yuan, J. F. Freimuth, and T. Jungwirth, Nat. Phys. **12**, 855 (2016).

[5] H. Ebert, S. Mankovsky, K. Chadova, S. Polesya, J. Minár, and D. Ködderitzsch, Phys. Rev. B **91**, 165132 (2015).

[6] D. Ködderitzsch, K. Chadova, J. Minár, and H. Ebert, New J. Phys. **15**, 053009 (2013).

[7] J. Staunton, B. L. Gyorffy, A. J. Pindor, G. M. Stocks, and H. Winter, J. Phys. F **15**, 1387 (1985).

[8] B. Gyorffy, A. Pindor, J. Staunton, G. Stocks, and H. Winter, J. Phys. F **15**, 1337 (1985).

[9] J. Kudrnovský, V. Drchal, I. Turek, S. Khmelevskyi, J. K. Glasbrenner, and K. D. Belashchenko, Phys. Rev. B **86**, 144423 (2012).

[10] V. Drchal, J. Kudrnovský, and I. Turek, EPJ Web Conf. **40**, 11001 (2013).

[11] J. K. Glasbrenner, B. S. Pujari, and K. D. Belashchenko, Phys. Rev. B **89**, 174408 (2014).

[12] A. A. Starikov, Y. Liu, Z. Yuan, and P. J. Kelly, Phys. Rev. B **97**, 214415 (2018).

[13] J. Kudrnovský, V. Drchal, and I. Turek, Phys. Rev. B **89**, 224422 (2014).

[14] J. Kudrnovský, V. Drchal, and I. Turek, Phys. Rev. B **88**, 014422 (2013).

[15] K. Carva, J. Kudrnovský, F. Máca, V. Drchal, I. Turek, P. Baláž, V. Tkáč, V. Holý, V. Sechovský, and J. Honolka, Phys. Rev. B **93**, 214409 (2016).

[16] F. Máca, J. Kudrnovský, V. Drchal, K. Carva, P. Baláž, and I. Turek, Phys. Rev. B **96**, 094406 (2017).

[17] S. Y. Bodnar, L. Šmejkal, I. Turek, T. Jungwirth, O. Gomonay, J. Sinova, A. A. Sapozhnik, H.-J. Elmers, M. Kläui, and M. Jourdan, Nat. Commun. **9**, 348 (2018).

[18] D. Wagenknecht, J. Kudrnovský, L. Šmejkal, K. Carva, and I. Turek, J. Magn. Magn. Mater. **474**, 517 (2019).

[19] D. Wagenknecht, K. Carva, and I. Turek, IEEE Trans. Magn. **53**, 1700205 (2017).

[20] D. Wagenknecht, K. Carva, and I. Turek, Proc. SPIE **10357**, 103572W (2017).

[21] D. Wagenknecht, I. Turek, and K. Carva, in *WDS'15 Proceedings of Contributed Papers—Physics*, edited by J. Šafránková and J. Pavlů (Matfyzpress, Praha, 2015), pp. 42–47.

[22] M. I. Katsnelson, V. Y. Irkhin, L. Chioncel, A. I. Lichtenstein, and R. A. de Groot, Rev. Mod. Phys. **80**, 315 (2008).

[23] R. A. de Groot, F. M. Mueller, P. G. van Engen, and K. H. J. Buschow, Phys. Rev. Lett. **50**, 2024 (1983).

[24] M. Otto, R. Van Woerden, P. Van der Valk, J. Wijngaard, C. Van Bruggen, C. Haas, and K. Buschow, J. Phys.: Condens. Matter **1**, 2341 (1989).

[25] W. Branford, S. Roy, S. Clowes, Y. Miyoshi, Y. Bugoslavsky, S. Gardelis, J. Giapintzakis, and L. Cohen, J. Magn. Magn. Mater. **272–276**, E1399 (2004).

[26] L. Ritchie, G. Xiao, Y. Ji, T. Y. Chen, C. L. Chien, M. Zhang, J. Chen, Z. Liu, G. Wu, and X. X. Zhang, Phys. Rev. B **68**, 104430 (2003).

[27] R. J. Soulen, J. M. Byers, M. S. Osofsky, B. Nadgorny, T. Ambrose, S. F. Cheng, P. R. Broussard, C. T. Tanaka, J. Nowak, J. S. Moodera, A. Barry, and J. M. D. Coey, Science **282**, 85 (1998).

[28] S. K. Clowes, Y. Miyoshi, Y. Bugoslavsky, W. R. Branford, C. Grigorescu, S. A. Manea, O. Monnereau, and L. F. Cohen, Phys. Rev. B **69**, 214425 (2004).

[29] G. Qu, P.-H. Cheng, Y. Du, Y. Sakuraba, S. Kasai, and K. Hono, Appl. Phys. Lett. **111**, 222402 (2017).

[30] G. Bona, F. Meier, M. Taborelli, E. Bucher, and P. Schmidt, Solid State Commun. **56**, 391 (1985).

[31] C. Morari, W. H. Appelt, A. Östlin, A. Prinz-Zwick, U. Schwingenschlögl, U. Eckern, and L. Chioncel, Phys. Rev. B **96**, 205137 (2017).

[32] J. Rusz, L. Bergqvist, J. Kudrnovský, and I. Turek, Phys. Rev. B **73**, 214412 (2006).

[33] J. Rusz, J. Kudrnovský, and I. Turek, J. Magn. Magn. Mater. **310**, 1654 (2007).

[34] S. Gardelis, J. Androulakis, P. Migiakis, J. Giapintzakis, S. K. Clowes, Y. Bugoslavsky, W. R. Branford, Y. Miyoshi, and L. F. Cohen, J. Appl. Phys. **95**, 8063 (2004).
[35] S. Ren, J. Gao, X. Jiang, G. Ji, W. Zou, F. Zhang, and Y. Du, J. Alloys Compd. **384**, 22 (2004).
[36] C. Hordequin, E. Lelievre-Berna, and J. Pierre, Physica B: Condensed Matter **234–236**, 602 (1997).
[37] J. Kudrnovský, V. Drchal, I. Turek, and P. Weinberger, Phys. Rev. B **78**, 054441 (2008).
[38] B. Alling, S. Shallcross, and I. A. Abrikosov, Phys. Rev. B **73**, 064418 (2006).
[39] C. Hordequin, D. Ristoiu, L. Ranno, and J. Pierre, Eur. Phys. J. B **16**, 287 (2000).
[40] I. Turek, V. Drchal, J. Kudrnovský, M. Šob, and P. Weinberger, *Electronic Structure of Disordered Alloys, Surfaces and Interfaces*, 1st ed. (Kluwer Academic Publishers, Boston, MA, 1997).
[41] E. F. Skelton and J. L. Katz, Phys. Rev. **171**, 801 (1968).
[42] G. Ouyang, Z. M. Zhu, W. G. Zhu, and C. Q. Sun, J. Phys. Chem. C **114**, 1805 (2010).
[43] B. Skubic, J. Hellsvik, L. Nordström, and O. Eriksson, J. Phys.: Condens. Matter **20**, 315203 (2008).
[44] S. K. Bose, J. Kudrnovský, V. Drchal, and I. Turek, Phys. Rev. B **82**, 174402 (2010).
[45] I. Turek, J. Kudrnovský, and V. Drchal, Phys. Rev. B **89**, 064405 (2014).
[46] K. Carva, I. Turek, J. Kudrnovský, and O. Bengone, Phys. Rev. B **73**, 144421 (2006).
[47] I. Turek, J. Kudrnovský, V. Drchal, L. Szunyogh, and P. Weinberger, Phys. Rev. B **65**, 125101 (2002).
[48] D. Orgassa, H. Fujiwara, T. C. Schulthess, and W. H. Butler, Phys. Rev. B **60**, 13237 (1999).
[49] I. Turek, J. Kudrnovský, and V. Drchal, Phys. Rev. B **86**, 014405 (2012).
[50] N. Mott, Adv. Phys. **13**, 325 (1964).
[51] C. N. Borca, T. Komesu, H. Jeong, P. A. Dowben, D. Ristoiu, C. Hordequin, J. Pierre, and J. P. Nozières, Appl. Phys. Lett. **77**, 88 (2000).
[52] S. Podgornykh, S. Streltsov, V. Kazantsev, and E. Shreder, J. Magn. Magn. Mater. **311**, 530 (2007).
[53] Y. Wu, B. Wei, Z. Zhou, C. Zhao, Y. Xiong, S. Tou, S. Yang, B. Zhou, and Y. Shao, Intermetallics **53**, 26 (2014).
[54] M. Pugaczowa-Michalska, Solid State Commun. **140**, 251 (2006).
[55] M. Otto, R. A. M. van Woerden, P. J. van der Valk, J. Wijngaard, C. F. van Bruggen, and C. Haas, J. Phys.: Condens. Matter **1**, 2351 (1989).
[56] P. Gumbsch and M. W. Finnis, Philos. Mag. Lett. **73**, 137 (1996).
[57] J. Baijal and U. Baijal, Phys. Lett. **23**, 67 (1966).
[58] S. Lowitzer, D. Ködderitzsch, and H. Ebert, Phys. Rev. Lett. **105**, 266604 (2010).
[59] K. S. Takahashi, H. Ishizuka, T. Murata, Q. Y. Wang, Y. Tokura, N. Nagaosa, and M. Kawasaki, Sci. Adv. **4**, eaar7880 (2018).
[60] N. Nagaosa, J. Sinova, S. Onoda, A. H. MacDonald, and N. P. Ong, Rev. Mod. Phys. **82**, 1539 (2010).
[61] J. Friedel, London Edinburgh Dublin Philos. Mag. J. Sci. **43**, 153 (1952).